Particle Physics at CERN

Annual Report 2001

C.Amsler, A. Dorokhov, A. Glauser, D. Grögler, O. Iannarelli, R. Kaufmann, D. Lindelöf, O. Link, N. Madsen, H.P. Meyer, K. Prokofiev, H. Pruys, C. Regenfus, P. Robmann, T. Speer, S. Steiner, and B. Wachter

Physik-Institut der Universität Zürich,
Winterthurerstrasse 190, CH-8057 Zürich, Switzerland

May 7, 2002

1 Production and Spectroscopy of Antihydrogen

C. Amsler, A. Glauser, D. Grögler, O. Iannarelli, D. Lindelöf,
N. Madsen, H.P. Meyer, H. Pruys, and C. Regenfus

In collaboration with: CERN, MIT, University of Aarhus, Brescia, Genoa, Pavia, Rio de Janeiro, Tokyo, Wales (ATHENA/AD-1 Collaboration).

1.1 Introduction

The physics goal of the ATHENA experiment [1] is a direct comparison of the properties of antihydrogen and hydrogen atoms (for a recent review, see ref. [2]). The final target is the most precise test of CPT invariance in the lepton and baryon sector. The long lifetime (122 ms) of the metastable (anti-) hydrogen 2S level is associated with a relative natural line width of 5×10^{-16} for the 1S-2S transition, which can be exploited by two-photon laser spectroscopy. In addition, such high precision measurements would give valuable experimental information on the gravitational interaction of antihydrogen, because a change in the 1S-2S transition frequency could also originate from a different redshift of antihydrogen and hydrogen atoms in the gravitational field of the earth. So far, only the existence of antihydrogen was demonstrated experimentally with the production of a few dozens of energetic antihydrogen atoms at LEAR [3] and at FNAL [4].

The current phase 1 of ATHENA is devoted to the formation of large quantities of antihydrogen atoms in Penning traps, with the goal of obtaining large rates (> 1 Hz) at the lowest possible kinetic energy ($<< 1$ eV). The formation rate depends on the densities of antiproton and positron plasmas, the absolute number of particles, their temperature, and on the trap potentials. The result of these studies will determine the apparatus of phase 2, the laser spectroscopic precision measurements.

The ATHENA apparatus was installed and commissioned in 1999/2000 at one of the three extraction lines of the new Antiproton Decelerator (AD) at CERN. The AD captures 5×10^{7} antiprotons at 3.5 GeV/c and decelerates them to 100 MeV/c (5.3 MeV kinetic energy), using stochastic and electron cooling, before extracting the antiproton bunch within 250 ns. Steady improvements by the AD team resulted in an intensity of 3–4$\times10^{7}$ antiprotons per spill, with a cycle time of 96 seconds. The number of antiprotons per bunch is now exceeding the value given in the design report.

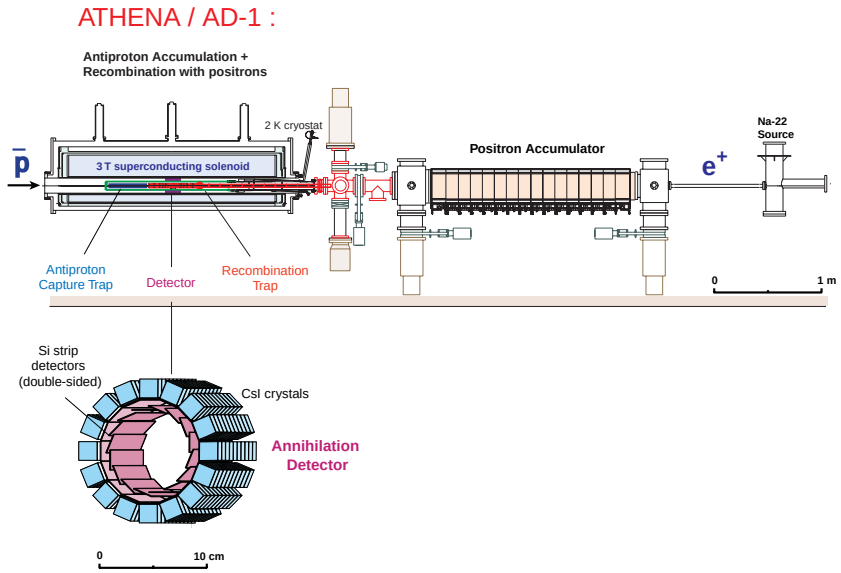

Figure 1.1: *Overview of the ATHENA apparatus for phase 1 (production of antihydrogen). A sketch of the detector designed by the Zürich group is shown below.*

1.2 Experimental setup

The apparatus (fig.1.1) consists of (i) an antiproton capture trap and a recombination trap, located in a cryogenic vacuum enclosure inside a large bore 3 T solenoid, (ii) a positron accumulator for collecting, cooling and transferring a large number of positrons ($> 10^8$) every 3–5 minutes to the recombination trap, and (iii) a high granularity large solid angle antihydrogen detector. More details on the apparatus are given in previous annual reports.

The incoming antiproton pulse is monitored by a 67 μm thin segmented silicon beam counter. The range of antiprotons with kinetic energy of 5.3 MeV is only about 200 μm in silicon. The amount of material in the beam was carefully optimized to obtain the maximum number of captured antiprotons by introducing a foil with variable tilt angle. The optimum thickness was determined by trapping antiprotons, releasing them after a delay of several seconds and measuring the number of annihilations. After determination of the optimal value, the tilted foil was removed and 44 μm of aluminium was added to the degrader material at the trap entrance.

The antiproton catching trap consists of cylindrical electrodes of various lengths and radii 1.25 cm made of gold-plated aluminium. Seven electrodes are used to create a harmonic field region in the capture region, three upstream and downstream to shape the electric field during various phases of particle transfer and handling, and two at the ends for applying the high voltage necessary to capture antiprotons. The exit electrode is biased to –10 kV. The entrance electrode (HVL) is quickly lowered to –10 kV, triggered by the signal from an external scintillator monitoring the arrival of antiprotons. We are able to capture about 20'000 antiprotons from a single AD shot of a few 10^7 antiprotons.

Before antiproton injection, a few 10^8 electrons are loaded from an electron source (heated filament). The electron cloud quickly cools down to ambient cryogenic temperature (10 K) by emitting synchrotron radiation. Antiprotons with energies in the keV range are then cooled within 20-30 s by interactions with the cold electrons stored in the central part of the catching trap. The lifetime of cooled antiprotons was measured to exceed ten hours. The high voltage electrodes could then be lowered to capture further $\bar{p}$ and several AD shots were successfully stacked.

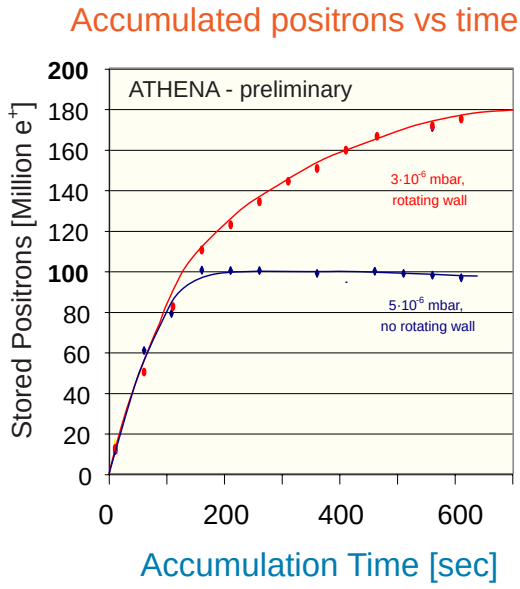

Figure 1.2: *Number of trapped positrons as a function of time, with and without rotating wall compression.*

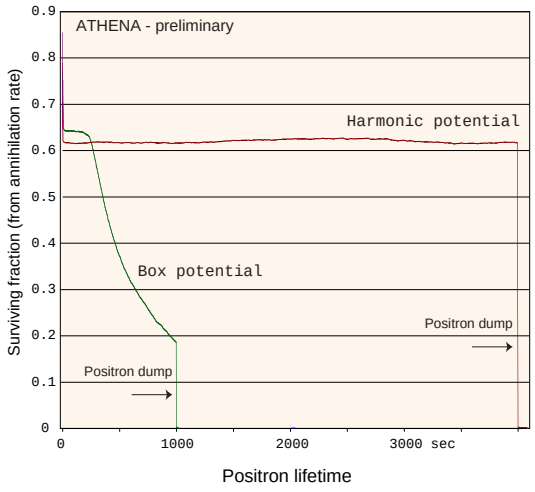

Figure 1.3: *Positron lifetime in the recombination trap, using a box potential or a harmonic trap potential.*

Positrons are emitted from a 50 mCi ^{22}Na source. After moderation in solid neon the low energy

beam of 7×10^6 positrons/s is guided into a 0.14 T magnetic field. The positrons enter an array of cylindrical electrodes, which have increasing radii and are biased at appropriate electric potentials. They are moderated by inelastic collisions with a nitrogen buffer gas. The size and radial position of the plasma is measured by dumping the positrons on a moveable, segmented Faraday cup detector. One of the trapping electrodes is split into six azimuthal segments to compress the plasma by applying a rotating electric field of several hundred kHz ("rotating wall"). During compression the plasma is cooled by the nitrogen buffer gas. The rotating wall technique reduces the diameter of the positron plasma from 15 to 4 mm. Figure 1.2 shows the number of positrons accumulated as a function of time: 1.7 $\times10^8$ positrons were accumulated in 450 seconds while without compression this number drops to about 10^8.

Positrons are transferred into the recombination trap by extracting the positron cloud from the accumulator trap: the buffer gas is pumped out and a magnet is turned on (1.2 T in 20 ms). The electrostatic trap is opened and the transfer electrodes are biased to accelerate the positrons towards the recombination trap. The transfer efficiency is measured by shooting the positrons directly on a Faraday cup and by measuring the annihilation signal with a CsI detector. Positrons are routinely transferred with efficiencies exceeding 50 %. The positrons are captured within 1s in the recombination region, where they cool by synchrotron radiation to the ambient temperature (10 K). Positron lifetimes of several hours have been achieved with a harmonic trap potential (fig. 1.3) and about 25 million trapped and cooled positrons were observed.

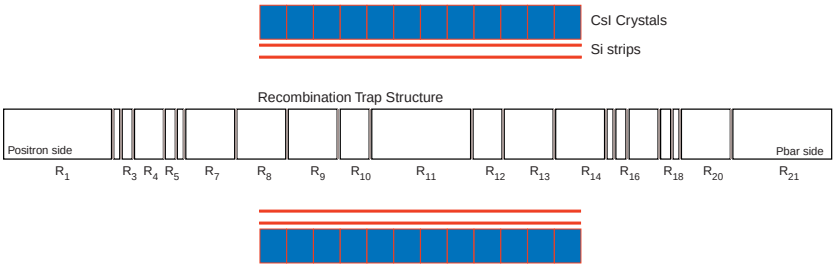

Figure 1.4: *Side view of the recombination trap and the antihydrogen detector.*

The recombination trap (fig. 1.4) consists of 21 cylindrical electrodes with a radii 1.25 cm and a total length of 41 cm. With this complicated structure we will be able to cool and compress the positron cloud with the rotating wall technique, store the anitiprotons transferred from the capture trap, overlap the antiproton and positron clouds, and monitor the plasma parameters (density, temperature).

The antihydrogen detector built by the Zürich group is now commissioned and is being used to detect antiproton and positron annihilations with the rest gas or the trap electrodes and to measure the position, size and shape of the plasma. The compact and highly granular detector measures the annihilation products of antiproton and positron annihilations. Since antihydrogen atoms are not confined by the electromagnetic fields of the recombination trap, they propagate freely and annihilate at the electrode surfaces after less than 1 ms. To maximize the detection efficiency, the detector is installed as close as possible to the recombination trap, inside the vacuum bore of the superconducting solenoid and around the cold nose containing the recombination trap system. Antiproton annihilation produces on average three charged pions and three high energy γ's while positron annihilation produces two 511 keV back-to-back photons (fig. 1.5). The charged pions are detected in two cylindrical layers of 16 double-sided silicon microstrip detectors (8192 channels) at average radii of 3.9 cm and 4.5 cm, respectively. The 511 keV photons from positron annihilation are detected by 16 rows of 12 pure CsI crystals (13 x 17.5 x 17 mm^3) read out by photodiodes. Figure 1.6 shows a photograph of the detector assembly. Details can be found in previous annual reports, diploma works [5] and in ref. [6].

A high granularity of the detector and good resolution on the photon energies are required by

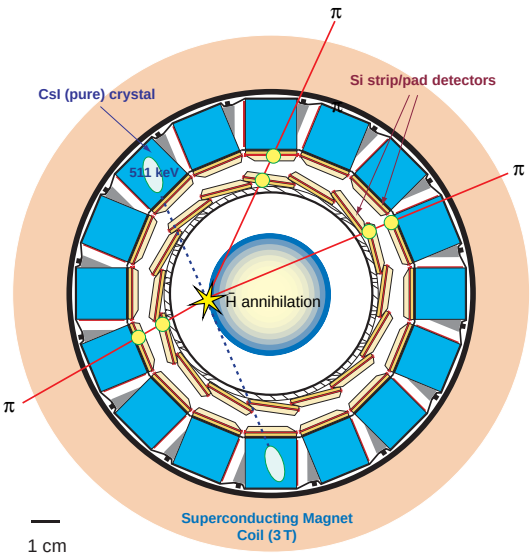

Figure 1.5: *Antihydrogen annihilation detector.*

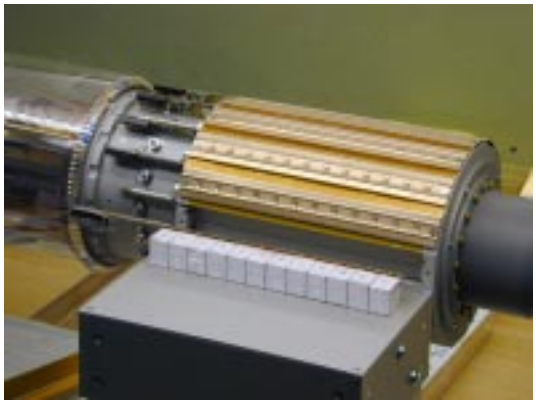

Figure 1.6: *Antihydrogen detector during assembly showing a row of crystals. .*

background considerations: antiproton annihilating on the electrode surface can fake antihydrogen annihilation, since high energy photons from the annihilation convert e.g. in the magnet coil, creating positrons which annihilate outside the detector region. This background can be suppressed by requiring the two back-to-back 511 keV photons to emerge from the annihilation vertex. The latter is determined from the tracks of the emitted pions and is required to lie at the electrode radius. The resolution on the annihilation vertex is 3 mm (r.m.s).

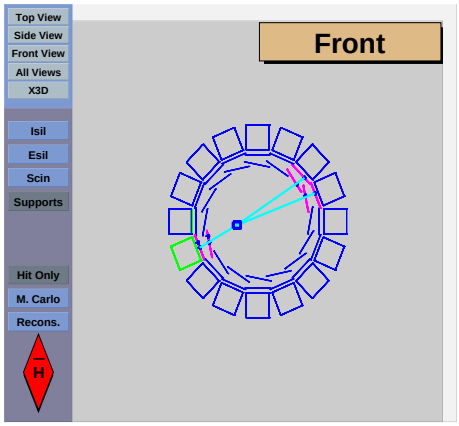

Figure 1.7: *Event display of a 3-prong annihilation event from a trapped antiproton hitting the cylindrical electrode. The hits in the strip detectors and the associated crystals are visible.*

The detector located inside the cold bore of the magnet is operated at a temperature between 77 and 140 K. The performance of pure CsI crystals and photodiodes (light yield and efficiency) were measured at low temperature: the photon yield at 80K is on average, 30'000 per MeV, as compared to 3'200 per MeV at room temperature. A record value of 50'000 per MeV was reported [6]. The first annihilations from antiprotons in the recombination trap were observed during summer 2001. Figure 1.7 shows a 3-prong annihilation event from a trapped antiproton.

The capability to measure the vertex of antiproton annihilations with rest gas atoms or on trap electrodes is a new tool for (destructive) plasma diagnostics. We can monitor the shape of the antiproton cloud and follow its evolution in time. Figure 1.8 shows the $\bar{p}$ annihilation vertex distribution in the recombination trap in three projections. Annihilations on a trap electrode at a radius of 1.25

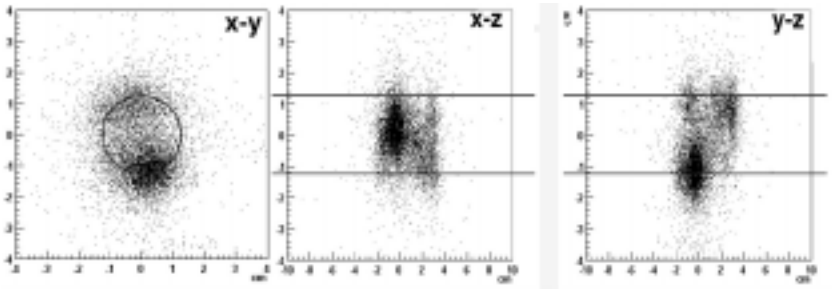

Figure 1.8: *Distribution of the antiproton annihilation vertices in the three projections; the z direction is the along the symmetry axis of the cylindrical trap. The lines show the boundary (wall) of the trap.*

cm are visible. Annihilations at smaller radii are due to collisions with rest gas atoms. The resolution of σ= 3–4 mm stems from the unknown track curvatures in the magnetic field (which cannot be measured with two layers of strip detectors) and is fully compatible with expectations.

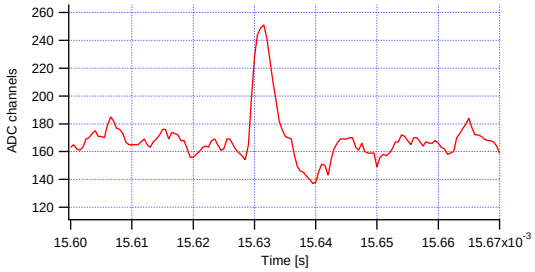

Figure 1.9: *Time signal from a 511 keV photon observed in one of the 192 CsI crystals of the antihydrogen detector surrounding the recombination trap filled with positrons at a temperature of 140 K.*

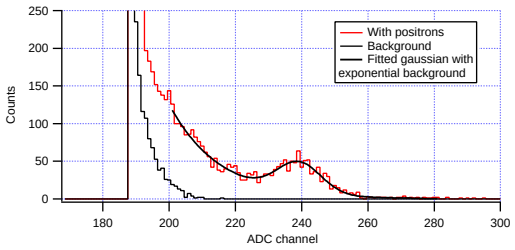

Figure 1.10: *γ-energy distribution in one of the CsI crystals when the trap is filled with positrons. The top distribution shows the spectrum from positron annihilation, with a clear peak at 511 keV, and a shoulder above background due to Compton scattered gammas. The bottom distribution shows the energy spectrum of background γ's.*

The transfer, capture and storage of positrons in the recombination trap can be monitored by measuring their annihilations with our CsI crystals. The annihilation signal from one of the 192 crystals is shown in fig. 1.9 and the energy distribution of the 511 keV γs in in fig. 1.10. The background spectrum is clearly separated from the 511 keV peak and its associated Compton edge.

1.3 Avalanche photodiodes

To reduce costs and also to match the surface of our crystals the photodiodes were manufactured from the same wafers as the silicon strip detectors, with very thin entrance windows to maximize the efficiency for detection of blue light from CsI. However, we discovered during the 2001 runs that the electronic noise from many of the SINTEF photodiodes had increased substantially, reaching unacceptable levels (signal over noise ratio of 5 or less) so that 511 keV photons could not be detected with the good resolution (better than 10 % [6]) achieved previously. The problem was traced to oxydation of the electrical contacts to the photodiode (possibly due to the iodine of CsI). Commercially available Hamamatsu pin-photodiodes were investigated as a backup solution but, unfortunately, the

yield of electron/hole pairs was found to be too small, essentially due to their much smaller sizes.

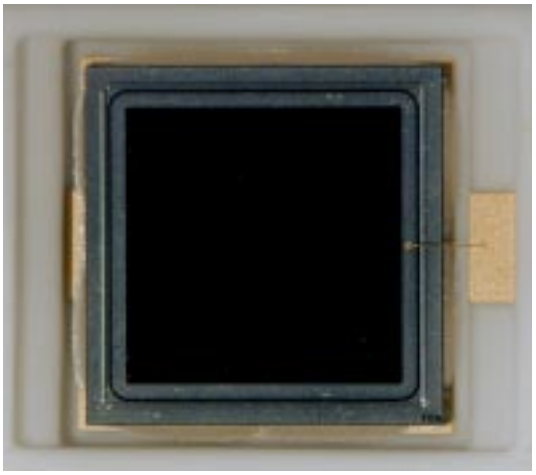

Figure 1.11: *Avalanche photodiode (5 × 5 mm^2) used for the CMS experiment with its epoxy window removed.*

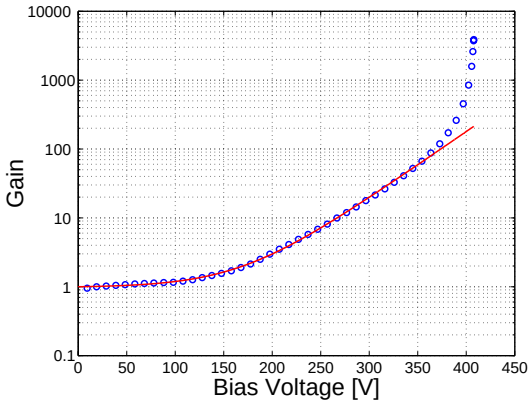

Figure 1.12: *Gain of an avalanche photodiode at room temperature as a function of bias voltage V. The curve is a fit with a function of the form* $a + b\,\exp(cV)$

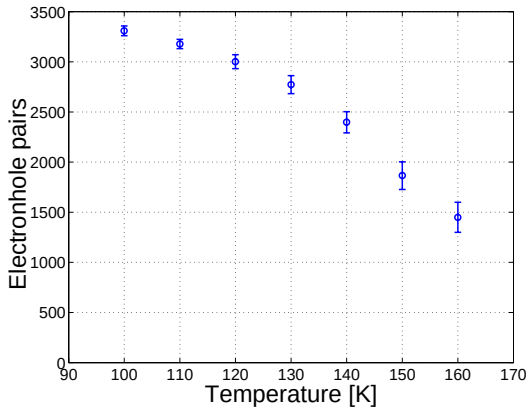

Figure 1.13: *Number of primary electron-hole pairs in the APD per 1 MeV energy loss in CsI, as a function of temperature.*

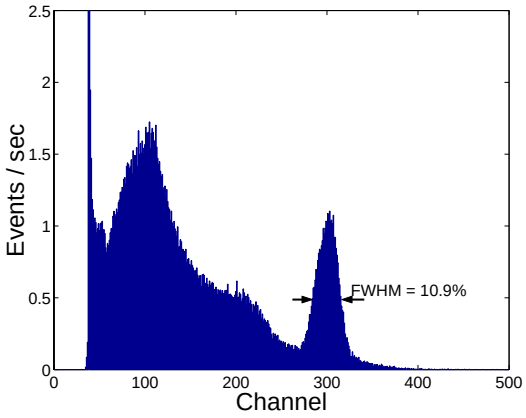

Figure 1.14: *γ-energy spectrum from one of the CsI crystals coupled to an APD, for 622 keV photons from ^{137}CsI at liquid nitrogen temperature. The photopeak is detected with a resolution of 10.9 % (FWHM), and the Compton plateau (shoulder) is clearly visible.*

As an alternative solution we tried avalanche photodiodes (APD) which have the advantage of a large gain and hence a much better signal-over-noise ratio. Encouraging tests were performed with spare APDs obtained from the CMS experiment not satisfying their stringent gain requirements. However, we first had to remove the epoxy windows which break at liquid nitrogen temperature. The best stripping agent was found to be sulfuric acid. Figure 1.11 shows a photograph of one of the 300 APD's purchased from CMS (a small batch from their 160'000 supply!). The gain of the APD as a function of bias voltage was measured with a pulsed (blue) light emitting photodiode (fig. 1.12). The plateau at low voltage corresponds to unit gain, the rise is due to the generated avalanche in the diode. The voltage at which multiplication starts depends on temperature. The advantage of APD's

for ATHENA is the very low dark current at low temperature, so that the signal can be amplified to very high values (with a gain of 10^4 a signal-over-noise ratio of the same order of magnitude can be reached for 511 keV photons!). The useful gain is however limited by our VA2 preamplifiers. We settled for a gain of 20 (compared to 50 for CMS) corresponding to a signal-over-noise ratio of about 100.

Figure 1.13 shows the number of electron-hole pairs produced for an energy loss of 1 MeV in the CsI crystals. The typical yield of about 3'000/MeV is much lower than our 30'000 with SINTEF diodes [6]. This is due to the much smaller size of the APD's (5×5 mm^2 compared to 17×13 mm^2) and also to the thin air gap between the diode and the crystal. However the energy resolution is now determined by the light collection efficiency while noise becomes negligible. The resolution is not significantly worse than that obtained with SINTEF diodes (fig. 1.14).

We also found that APD's were much more sensitive to the blue component of light than to the red one. Therefore the red dye used previously as wavelength shifter to coat the crystals was removed and all SINTEF diodes replaced by APDs for the forthcoming 2002 runs.

1.4 Summary and outlook

To summarize, in 2001 ATHENA demonstrated the trapping, cooling and transfer to the recombination trap of 2×10^4 antiprotons. Several antiproton shots were stacked in the antiproton capture trap where a lifetime of 10 hours was measured. This allows us to reach the target of 10^5 stored and cooled antiprotons. In the positron accumulator we accumulated 1.5×10^8 positrons in five minutes which corresponds to an increase by two orders of magnitude with respect to the previous year. The transfer of 10^8 positrons from the accumulator to the recombination trap was demonstrated. Trapping and cooling led to 2.5×10^7 positrons with a lifetime of several hours. The target of 10^8 stored and cooled positrons is thus within reach.

The main goal for the coming year is to store simultaneously 10^5 antiprotons and 10^8 positrons in the recombination trap. We will search for annihilation of antihydrogen atoms hitting the electrodes using the antihydrogen detector. We will drive the antiprotons through the positron plasma with a frequency which maximizes the spontaneous antihydrogen formation rate while keeping the positron temperature as low as possible. Once the production of antihydrogen has been demonstrated we will measure its production rate as a function of plasma density and temperature, number of particles and trap potentials. Based on the $\bar{p}$ and e^+ intensities given above and on theoretical models of spontaneous radiative recombination, we expect the production of about 0.1 to 1 antihydrogen atoms per second. Depending on the yield of anti-atoms with very low kinetic energy ($<$0.05 meV), the optimal setup for a 1S-2S precision experiment will be designed. Meanwhile the Zürich group is involved in the preparation of the laser system, in particular the frequency doubler to produce the 243 nm light inducing the 1S to 2S transition by recoilless two-photon absorption. The year 2002 promises to be very exciting.

References

[1] ATHENA proposal, M.H. Holzscheiter et al., CERN-SPSLC/P302, October 1996, see also http://www.cern.ch/athena/

[2] M. H. Holzscheiter and M. Charlton , Rep. Prog. Phys. 62, 1 (1999); see also C. Amsler et al., *Antihydrogen Production and Precision Spectroscopy with ATHENA*, in "The Hydrogen Atom, Precision Physics of Simple Atomic Systems", edited by S.G. Karshenboim et al., Springer Lecture Notes in Physics, Berlin, 2001, p. 469-488.

[3] G. Baur et al., Phys. Lett. B368 (1996) 251.

[4] G. Blanford et al., Phys. Rev. Lett. 80 (1998) 3037.

[5] P. Niederberger, *Untersuchung von CsI-Szintillatoren bei tiefen Temperaturen*, Universität Zürich, 1999; R. Brunner, *Aufbau und Test eines Microstrip-Detektors für das ATHENA-Experiment*, Universität Zürich, 2000; D. Grögler, *Temperature Dependence of Pure CsI between 77 K and 165 K and the Performance of Wavelength Shifters* Universität Zürich, 2000.

[6] C. Amsler et al., Nuclear Instr. and Methods in Physics Research A 480 (2002) 492.

2 Particle Physics with CMS

C. Amsler, A. Dorokhov, R. Kaufmann[‡], K. Prokofiev, H. Pruys, C. Regenfus,
P. Robmann, T. Speer, and S. Steiner

In collaboration with: ETH-Zürich, Paul Scherrer Institut (PSI), Universität Basel
and the CMS Collaboration.

[‡] Now at CSEM, Switzerland

2.1 Introduction

We participate in the CMS experiment at the Large Hadron Collider (LHC) where we shall concentrate on physics involving the b-quark, e.g. b-quark production associated with the formation of Higgs bosons, t-quark decays, spectroscopy of B mesons and CP violation in B decays. For a low mass Higgs, below about 135 GeV, the dominant decay mode is $H^0 \rightarrow b\bar{b}$. The tagging of b-jets is also essential for the detection of the top quark as, V_{tb} being essentially one, the top quark decays nearly exclusively to W^+b. The study of the rare decays $t \rightarrow W^+d$ and $t \rightarrow W^+s$ gives a direct measurement of the CKM matrix elements V_{td} and V_{ts} and hence, in case unitarity is violated, leads to physics beyond the Standard Model. Also, searches for flavor changing neutral currents in rare B-decays, like B_d or B_s to $\mu^+\mu^-$, are forbidden at the tree level, but may occur at higher orders and therefore allow to test the Standard Model and to probe its extensions at low energy.

The most interesting events at LHC will therefore contain one or several b-jets originating from the decay of B mesons, with typical mean free paths of a few mm. To allow for efficient tagging of B mesons among the large background of light quark and gluon jets, the detection system has to follow particles towards the primary vertex. In fact, our pixel detector, the closest detector to the interaction point, will be located only 4 cm from the beam-beam interaction point. The extremely high particle flux near the primary vertex ($\sim$ 1000 particles every 25 ns, see fig.2.1) requires the innermost tracking layers to be composed of pixel devices delivering 3D coordinates with high resolution and no ambiguity. Furthermore, the radiation dose to the nearest detector will approach 10^6 Gy (corresponding to 6×10^{14} hadrons /cm^2) after 10 years of LHC operation (fig.2.2). This is about 10^6 more than for detectors developed earlier for space research.

Our group joined the CMS collaboration in 1995. During the following years we contributed [1, 2, 3] to the development of the pixel detector, the specifications of which are given in the Technical Design Report [4]. We are also responsible for the design and delivery of the mechanical support structure and the service tubes that will transfer the power, the signals and the coolant to the detector. We are participating in the reconstruction software and physics simulation involving the charged particle tracker. In 2000/2001 we initiated a study of various designs for pixel sensors [5] (which will be briefly discussed below) and, recently, we embarked on tests of the readout chips for the pixel sensors.

2.2 The pixel sensors

The CMS pixel detector (fig. 2.3) is made of three cylindrical layers, 53 cm long, with radii of 4.3, 7.1 and 11 cm (fig. 2.3, and Table 2.1). The barrel layers containing some 3×10^7 silicon pixels will be provided by the ETH-PSI-Basel-Zürich collaboration while the forward/backward wheels will be supplied by the U.S. participants. The pixel modules consist of thin, segmented sensor plates with highly integrated readout chips connected by the indium bump bonding technique (fig.2.4). A sensor plate contains 53×52 pixels, each with a surface area of 150×150 μm^2 and a thickness of 200 μm. The analog signals are read out to determine the coordinates more accurately, using charge sharing between adjacent pixels in the strong magnetic field of CMS.

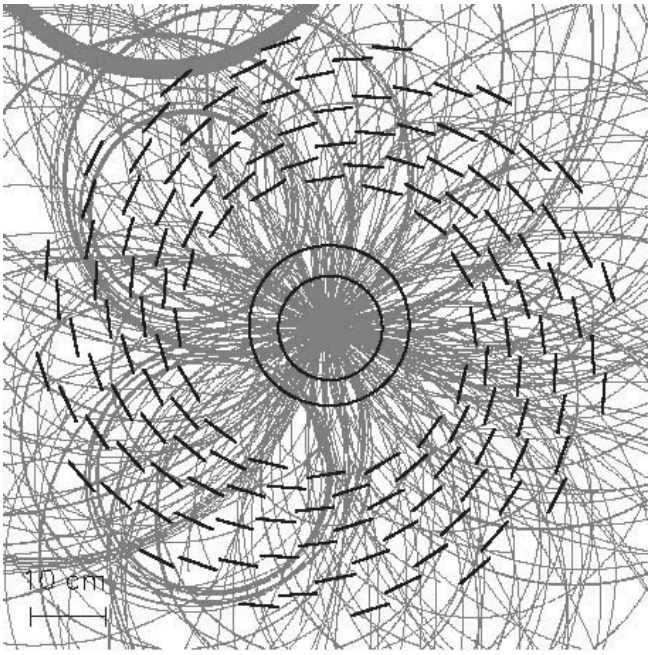

Figure 2.1: *Interesting events will have to be filtered from events with on average 18 superimposed interactions occuring during the same bunch crossing time. The event shown is a simulated Higgs decay* $H \rightarrow Z^0 Z^0 \rightarrow 2(\mu^+\mu^-)$*. The circles show the two innermost pixel layers, the circle segments represent the microstrip silicon tracker.*

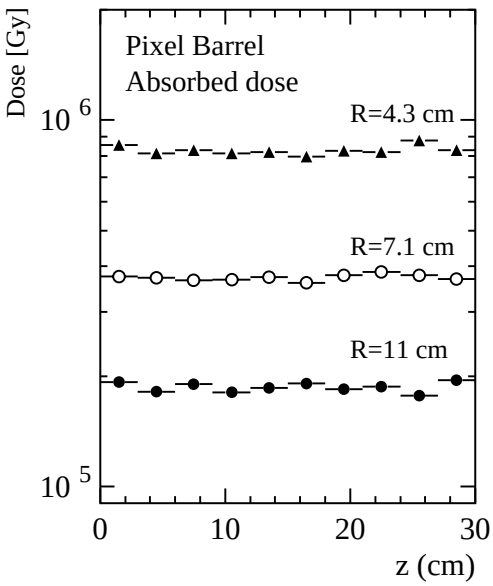

Figure 2.2: *Expected dose absorbed by the CMS pixel barrel in the three layers (radii R), as a function of coordinate along the beam axis (for 10 years of LHC operation).*

The bulk of the sensor is n-material and the implants are n^+. The negative bias voltage is applied to the backside and hence the readout signal is generated by electrons. The depletion layer grows from the backside (p^+ layer) and reaches the n^+ implants at full depletion (typically 150 V and up to several 100 V for irradiated devices). However, after irradiation, type inversion occurs (due to displacements of atoms in the lattice) and hence the depletion layer grows from the n^+ side. The guard rings ensure a smooth decrease of the bias potential over the edge so that the high field region does not reach the n^+ side which is at ground potential with the readout chip. For n^+ implants in n-material the pixels have to be isolated from one another. This is usually done with one or several narrow p^+-rings around each pixel (the so-called p-stop rings). To avoid excessive charging of an unbonded pixel (one with poor indium connection to the chip), leading to local discharges and momentary failures of whole pixel clusters, the resistance between pixels should remain finite. A narrow resistive path between the pixels would prevent the pixels from charging up. This is accomplished by small openings in the

Table 2.1: *Number of channels and rates at the design luminosity of* $10^{34} cm^{-2} s^{-1}$.

	Barrel (r)			End cap (z)	
Layer	4 cm	7 cm	11 cm	33 cm	47 cm
Number of chips	2340	2840	5888	1080	1080
Number of pixels	6.35×10^6	10.6×10^6	16.2×10^6	3.0×10^6	3.0×10^6
Area	0.15 m^2	0.25 m^2	0.38 m^2	0.07 m^2	0.07 m^2
Pixel hit rate	24.0 kHz	10.3 kHz	6.9 kHz	lower	

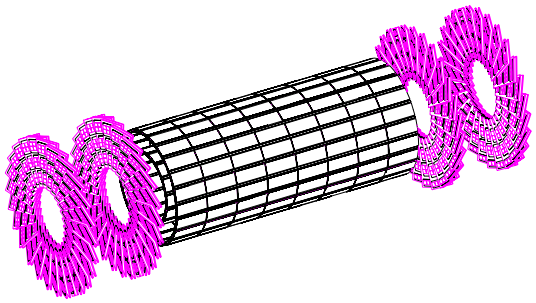

Figure 2.3: *Perspective view of the CMS pixel detector.*

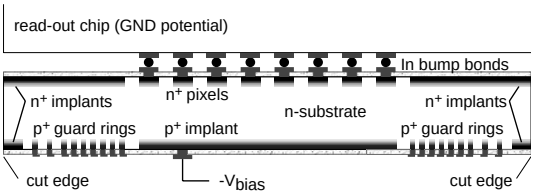

Figure 2.4: *Design of a sensor plate connected to the readout chip. The bias voltage is applied to the backside.*

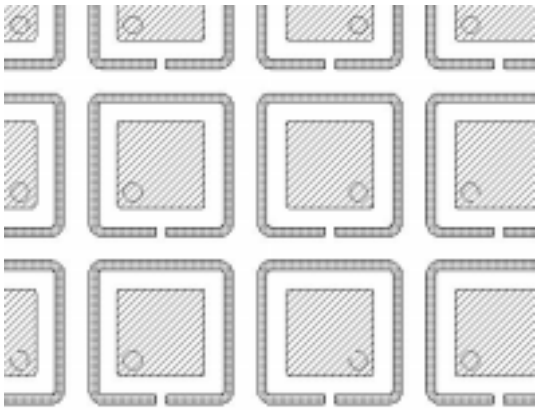

Figure 2.5: *Sensor design with one p-stop ring surrounding the pixels. The sizes of the n^+-implants and the spacings are typically 75μm and 10 μm, respectively.*

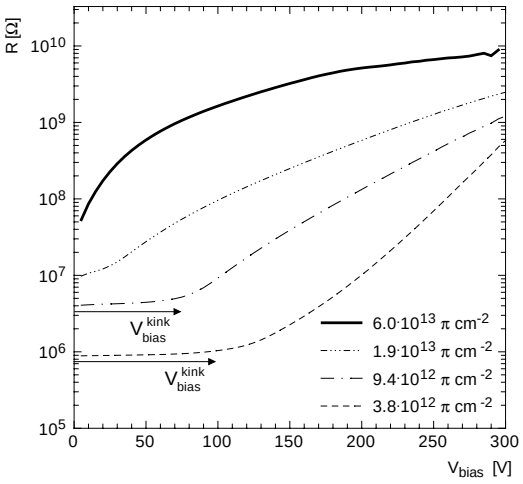

Figure 2.6: *Interpixel resistance as a function of bias voltage, for various particle fluxes. The kink in the bias voltage vanishes when type inversion occurs.*

p-rings which lead to atoll-like structures. Figure 2.5 shows our favorite design for the elementary sensor cell.

During 2001 we performed many tests on the sensor designs that were submitted to SINTEF (Oslo) and CSEM (Neuchâtel) [5]. A sample of 16 layouts, including various p-stop ring geometries and guard rings, were produced on 24 wafers with different resistivities. We inspected the planarity of the delivered devices, performed leakage current and $C-V$ measurements with a probe station, and determined from the depletion voltage the doping concentration (donor concentration in the bulk, 2×10^{12} cm^{-3}). In the implants the concentration was determined to be $n^+ = 10^{18}$ cm^{-3}. The resistance between pixels (interpixel resistance), relevant for the insulation between them, was found to be typically a few MΩ, depending on the p-stop ring design.

Some of the devices were then irradiated with protons at the ROSE facility at CERN, and with pions at PSI. We determined the radiation dose at which type inversion occurs: after type inversion there is no flat interpixel resistance regime as a function of bias voltage, as there is no undepleted zone between the implants (the depletion layer grows from the n^+ side). For CSEM (SINTEF) devices type inversion occurs at a dose of 2.1×10^{13} (3.6×10^{13}) hadrons cm^{-2} (the expected radiation dose is 6×10^{14} after 10 years of LHC operation). The resistance is shown in fig. 2.6 for several irradiation

doses. One finds that the interpixel resistance rises dramatically with dose, reaching several GΩ at full irradiation. Nonetheless, a beam test with an irradiated bump-bonded sensor behaved satisfactorily and did not show stochastic discharges in spite of this very high resistance.

We also measured the pixel capacitance (25.8 ± 1.8 fF, in good agreement with calculations) between a pixel and its neighbours and the backplane, by connecting many pixels in parallel. This result is very important for readout noise considerations.

From these and other R &D investigations [5] we concluded that the pixel detector envisaged in the proposal [4] was feasible. In 2002 we will investigate oxygen enriched sensors, for which the radiation hardness is increased due to the reduced acceptor concentration in n-type silicon [6].

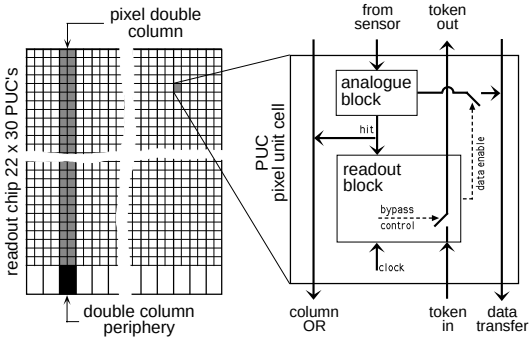

Figure 2.7: *Schematic of the PSI34 readout chip.*

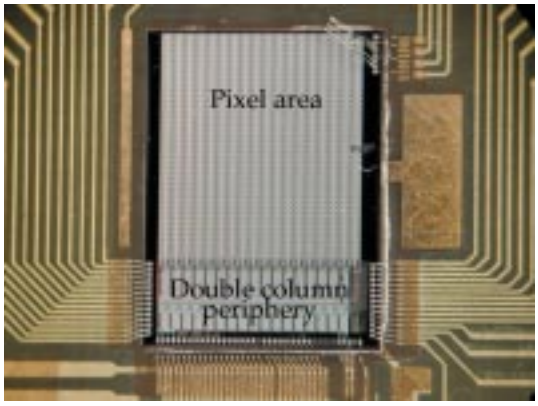

Figure 2.8: *Readout chip (version DM-PSI41) bonded to a test printed circuit board.*

2.3 Tests of the readout chip

Figure 2.7 explains the principles of the pixel readout chip (developed at PSI). The pixels are grouped in double columns, with a common bus to a double column periphery which controls the chip. The chips are produced in the radiation hard DMILL SOI (silicon on insulator) technology. Each pixel has its pixel unit cell (PUC), which consists of an analog and a digital block. It is equipped with a comparator allowing individually adjustable thresholds. Whenever a PUC detects a signal above threshold it stores the analog signal in a capacitor and notifies the double column periphery, which copies a time stamp into memory and requests a readout. A readout token is then sent through the chip and all double columns with hits are read out.

Each pixel is hit at an average rate of 10 kHz, and the information (address and collected charge) has to be stored for 3.2 ms in the front end part of the pixel readout electronics (fig. 2.8), until it is read out or discarded by the external readout electronics. The front end part of the electronics consists of the following parts: readout chip (ROC), line drivers, I^2C interface for controlling, token bit manager chip (TBM). Each readout chip reads out 2756 pixels (53 columns × 52 rows), and 16 readout chips are controlled by one token bit manager chip. The read out chip contains analog preamplifiers, shapers and discriminators, column periphery, readout buffers/amplifiers.

The analog preamplifier is made of two integrating amplifiers and one differentiating stage. Last year a preliminary version of the readout chip (DM-PSI41) was tested in our lab. Several parameters (supply voltages) were optimized to get acceptable gain, peaking time and low power dissipation. Different versions of the preamplifier were therefore produced on the same silicon substrate and bonded to printed circuit boards. The gain at the output of the amplifier is defined as the ratio of the peak amplitude to the injected input charge (fig. 2.9). The peaking time is defined as the time interval between the signal start and its peak value. The minimum power consumption was determined as a

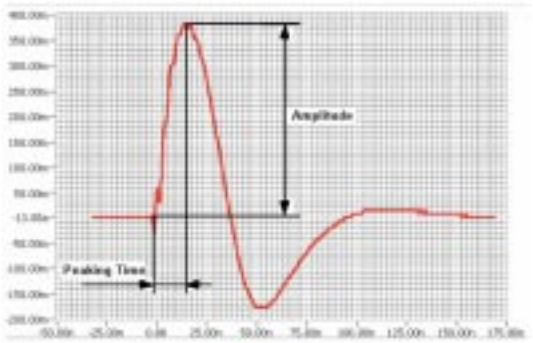

Figure 2.9: *Amplifier output signal.*

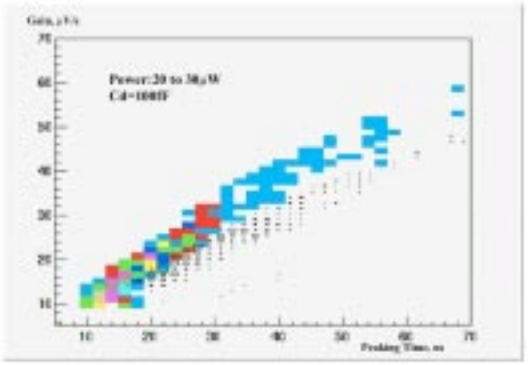

Figure 2.10: *Distribution of power dissipation as a function of peaking time for two different supply voltages (colored and black empty squares). The first version (colored squares) has a higher gain for the same power consumption and peaking time and is therefore superior.*

function of gain and peaking time by varying the supply voltages to the amplifiers. The distribution of power dissipation as a function of gain and peaking time is plotted in (fig. 2.10). It is typically 25 μW per channel.

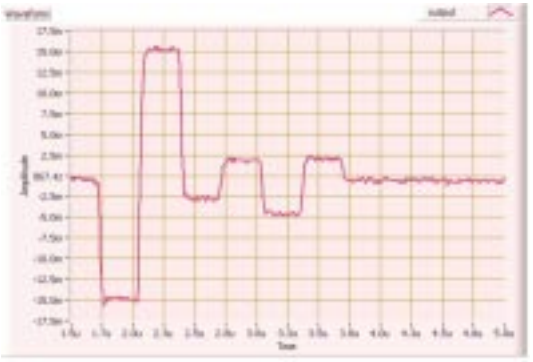

Figure 2.11: *Readout chip output for one hit pixel. The six bins encode the address and the charge collected by the pixel (see text).*

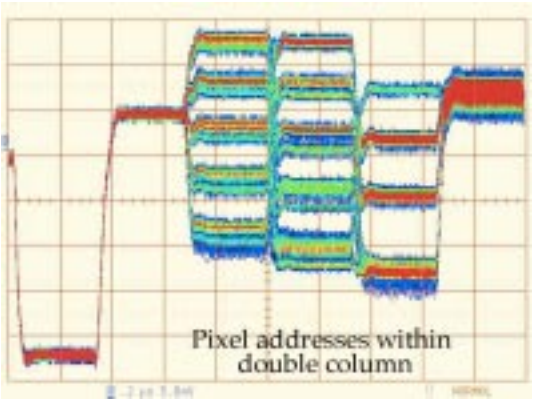

Figure 2.12: *Superposition of 80 signals from different pixels of the same double column. The first two bins have the same pulse height (same double column address). The next three are the five levels of pixel addresses within the double column.*

We also tested the digital part of the readout chip DM-PSI41 with a digital pattern generator DG2020 and a PCI digital I/O card. Because of the expected huge data rates at LHC (32 Gb/s), a 5-level logic is used instead of binary logic. For each hit pixel, the readout chip produces a signal (shown in fig. 2.11), which can be divided into six bins. The first five bins encode the pixel address while the sixth represents the analog signal from the pixel. The first two bins encode the double column address and the next three encode the pixel address within the double column. With five levels a total of $5^5 = 3125$ pixel addresses can be encoded by one readout chip. Figure 2.12 shows

the output for 80 superimposed signals from different hit pixels.

2.3.1 Simulation and reconstruction software

The Zürich group has taken major responsibilities in the development of the reconstruction software. With the high luminosity of the LHC, the challenge is to reliably find tracks in a high density environment (see the typical event of fig. 2.1 above), where low luminosity events will feature around 5000 hits and high luminosity events ten times more. Combinatorial problems can thus be severe, and the challenge is to find for each track the correct combination of hits in a reasonable amount of time. Tracks usually leave between 8 and 15 hits in the tracker (pixel and silicon detectors), depending on rapidity.

Figure 2.13 shows the new cms121 layout of the silicon tracker. We discovered that the transverse momentum resolution of high-p_t single muon tracks deteriorated significantly (Figure 2.14) when the microstrip gas chambers (cms118 layout) were replaced by the current all-silicon configuration. We conducted an analysis to trace the origin of this deterioration. It was attributed to the removal of one layer, reducing the average track length by 10 cm, to the gap between the outer barrel and the endcap detectors, and to a degradation of the resolution in the last rings of the disks.

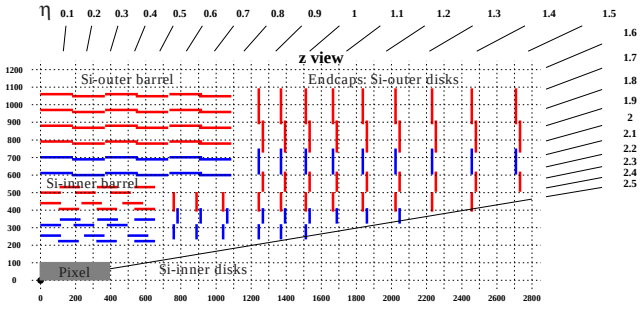

Figure 2.13: *The current cms121 all-silicon layout of the tracker; red, single-sided, blue double-sided readout. The parameter η denotes the pseudorapidity.*

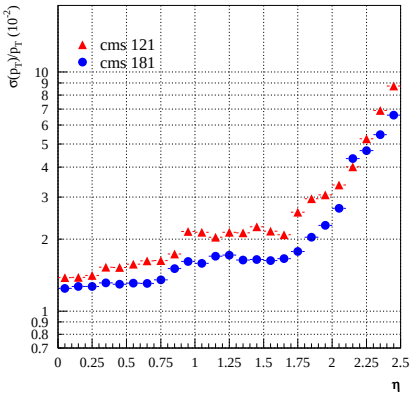

Figure 2.14: *Transverse momentum resolution of single muon tracks with p_t=100 GeV/c as a function of pseudorapidity η, predicted in the cms118 and cms121 configurations.*

A possible improvement was to reduce the average pitch of the sensors in the 7th (last) ring of the endcap disks from 156 to 104 μm. The effect on mass resolution was studied on the decay $H \rightarrow Z^0 Z^0 \rightarrow 2(\mu^+\mu^-)$. No improvement was observed since muons from Higgs decay are emitted with relatively low transverse momenta (below 50 GeV/c), where the resolution is dominated by multiple scattering. On the other hand, improvements on the mass resolution are possible for higher mass objects ($\sim$ 400 GeV) for which the decay momentum spectrum is harder. These states are, however, not expected to be narrow.

We also tried to increase the pitch of the sensors of the first two Outer Barrel layers from 122 to 133 μm. This would lower the number of readout chips by 2160 units. This modification would have little influence as it affects only hits in the middle of the tracks. It could, however, affect the effeciency of the pattern recognition. This was studied with b and τ jets. Pitch increase in the first

two Outer Barrel layers turn out to have little effect, the track reconstruction efficiency remaining essentially unchanged. Accordingly, the pitch will be increased in these layers to reduce costs.

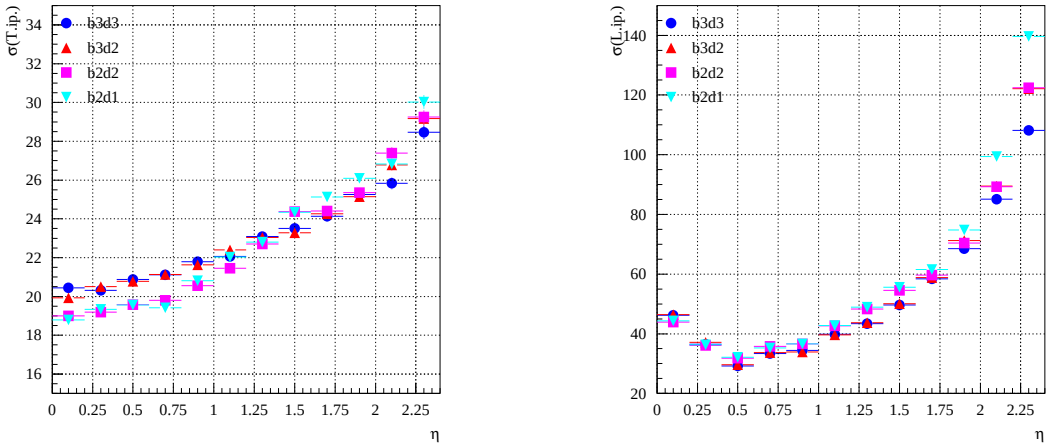

Figure 2.15: *Resolution of the transverse (left) and longitudinal (right) impact parameter (in μm) as a function of the pseudo-rapidity η for different configurations and 10 GeV/c muons.*

We studied several alternatives for the number of pixel layers which were discussed at a workshop in December 2001. The resolution on transverse momentum depends slightly on the radius of the innermost layer, as it is mostly determined by the total length of the track. The resolution on the azimuthal angle ϕ in the barrel improves slightly with the number of layers, but the resolution on the polar angle improves significantly, both in the barrel and in the endcaps. At high momentum the resolution on the transverse impact parameter (fig. 2.15, left) improves with the number of barrel layers, but shows no significant dependence on the number of disks. However, at low momentum, the resolution is best with two barrel layers, due to the reduction of material thickness. The resolution on the longitudinal impact parameter (figure 2.15, right) shows little dependence on the number of barrel layers but improves dramatically with the number of endcap disks. No dramatic change was observed, the layout with the largest number of layers offering the best performance. The pixel system will therefore consist of three barrel layers and two pairs of endcap disks.

We also studied the detection efficiency as a function of LHC bunch length. At injection the length of the longitudinal beam overlap is about 11 cm (FWHM). From experience with $\bar{p}p$ collisions at the SPS collider this length will increase to 18 cm (FWHM) after 10 hours of coasting beams.

To estimate the coverage in $\eta - \phi$ of each layer as a function of vertex position, muons with a transverse momentum of 100 GeV/c were generated with a uniform $\eta - \phi$ distribution and a vertex z-coordinate between between -30 and 30 cm. The coverage of the barrel pixel layers is fortunately not sensitive on the vertex position. The inefficiency is 2.9% in each layer (fig. 2.16, left), resulting mainly from the longitudinal gaps between the pixel modules, see fig. 2.16 (right). The coverage of the forward disks is, as expected, strongly dependent on the vertex position, and the total inefficiency is about 2%, mainly due to the radial gaps between the pixel modules.

In 2002 we will complete the improvements on the tracker geometry and tackle the vertex reconstruction. Our aim is to study and implement robust secondary vertex fit procedures, which are not sensitive to tracks that have a small probability to emerge from the secondary vertex.

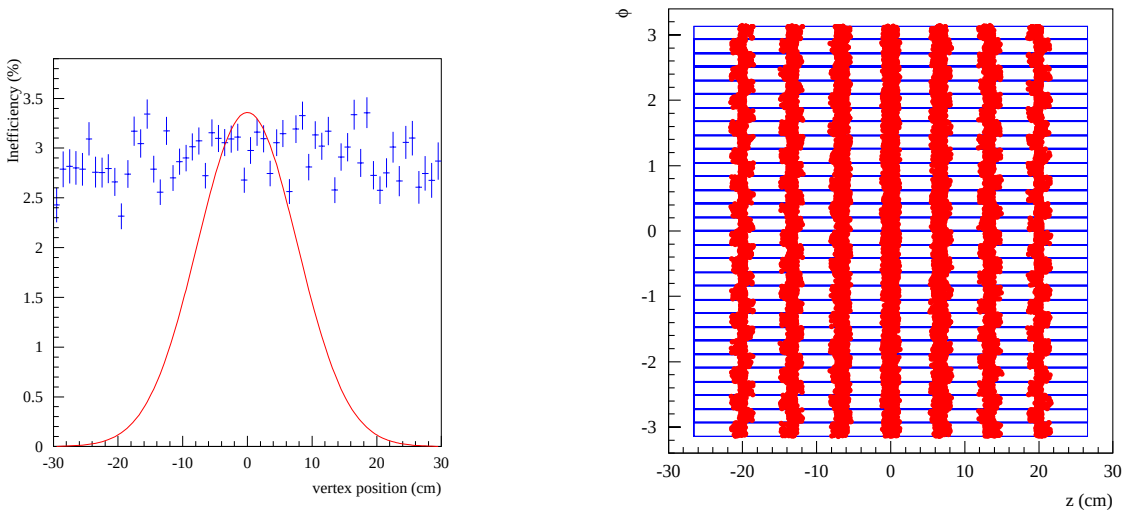

Figure 2.16: *Inefficiency as a function of vertex position for the second barrel pixel layer (left) and expected distribution of collision points after 10 hours of coasting beams (curve); right:* $\phi - z$ *view of the detector modules showing the missing hits in the second barrel pixel layer.*

References

[1] V. Dubacher, *Test of a Silicon Pixel Detector with 50 GeV Pions*, Universität Zürich (1996); R. Kaufmann, *Performance of a Silicon Pixel Detector in a Magnetic Field*, Universität Zürich (1997); M. Glättli, *Untersuchung von Silizium-Pixeldetektoren mit einem Silizium-Mikrostreifen-Strahlteleskop*, Universität Zürich (1998)

[2] G. Bolla et al., Nucl. Instr. Meth. in Phys. Research A 461 (2001) 182

[3] B. Henrich, R. Kaufmann, Nucl. Instr. Meth. in Phys. Research A 304 (2002) 304

[4] The Tracker Project, Technical Design Report, CERN LHCC 98-6, CMS TDR 5 (1998)

[5] R. Kaufmann, PhD thesis, Universität Zürich (2001)

[6] M. Moll, E. Fretwurst, G. Lindström, Nucl. Instr. Meth. in Phys, Res. A 439 (2000) 282

3 Measurement of the Neutrino Magnetic Moment at the Bugey Nuclear Reactor

C. Amsler, O. Link and T. Speer

In collaboration with: Institut des Sciences Nucléaires (Grenoble), Université de Neuchâtel, Università di Padova (MUNU Collaboration).

3.1 Introduction

In the standard model the magnetic moment vanishes for massless neutrinos. Even for massive ν_e with masses in the range observed recently, the standard model predicts magnetic moments much below 10^{-20} μ_B, which are not accessible experimentally. The experimental evidence for a large magnetic moment would mean new physics beyond the standard model. With a finite magnetic moment the spin of a lefthanded neutrino may flip due to the electromagnetic interaction, and the neutrino become a "sterile" righthanded state which does not interact, and hence is experimentally invisible. The precession of a magnetic moment in the range $\mu_\nu \sim 10^{-10} - 10^{-12}$ μ_B in the solar magnetic field offers an alternative explanation to the MSW effect for the observed deficit of solar neutrinos.

We measure the magnetic moment of antineutrinos $\overline{\nu}_e$ from a nuclear reactor, using the elastic scattering reaction $\overline{\nu}_e e^- \rightarrow \overline{\nu}_e e^-$. This process is very sensitive to the magnetic moment of the $\overline{\nu}_e$ (especially at low neutrino and low electron recoil energies) because it is a pure leptonic and theoretically well understood weak process. A finite neutrino magnetic moment leads to an excess of forward scattered low energy electrons.

A detailed description of the apparatus can be found in ref. [1, 2] and in previous annual reports. MUNU uses a 1 m^3 time projection chamber (TPC, gaseous CF_4 at 3 bar) surrounded by a tank filled with liquid scintillator to guard against cosmic muons and Compton scattering of low energy γs. We measure both the angle and the energy of the recoil electron and hence can calculate the neutrino energy. The energy threshold for detecting electrons is typically 300 keV. We also measure simultaneously the signal and the background, since electrons cannot be scattered in the backward hemisphere.

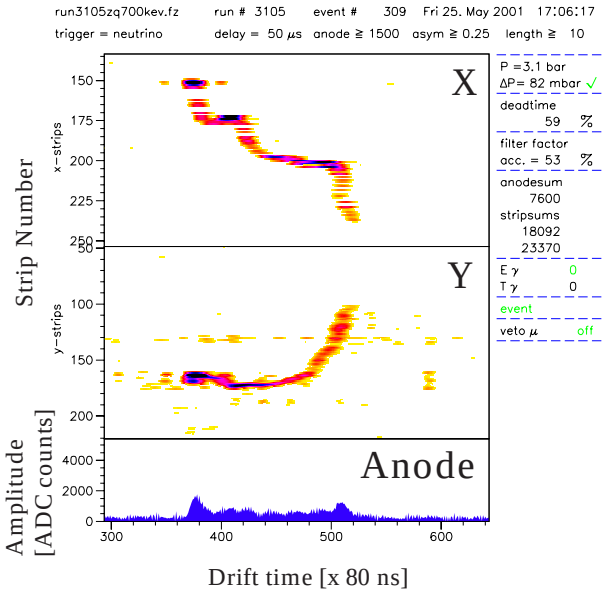

Figure 3.17: *Typical neutrino-electron scattering event visualized in the MUNU TPC. Shown are the x-z and y-z projections and the pulse height measured on the anode (bottom). Note the high ionization rate of the electron at the end of its track (black blob).*

3.2 Data analysis

The experiment works well since the beginning of 2001. We collected neutrino data during 111 days, corresponding to 68 days after deadtime subtraction. We also collected reactor off data during 37 days (24 days after deadtime subtraction). In addition, calibration data were recorded periodically for various triggers. A typical event is shown in fig. 3.17.

The data are being analysed following two different routes. In the first procedure ("visual" tracking, applied by the Neuchâtel group) every potential neutrino event is examined by eye and the scattering angle and recoil energy is determined. We briefly discuss the results from 30 days of neutrino runs with a high offline electron threshold of 700 keV. The lefthand side of fig. 3.18 shows the energy distribution of the recoil electrons for forward emission, i.e. for electrons emitted in the direction opposite to the reactor core. The distribution for backward electrons is also shown. Backward electrons do not stem from neutrino-electron scattering. Assuming that they are isotropically distributed we can subtract the two spectra to obtain the contribution from the signal events (fig. 3.18, right). The spectrum shows the expected shape, rising towards low electron energies. We obtain 95 ± 20 neutrino events for 30 days, while expecting 51 for a vanishing neutrino magnetic moment. We thus observe roughly twice as many events as predicted.

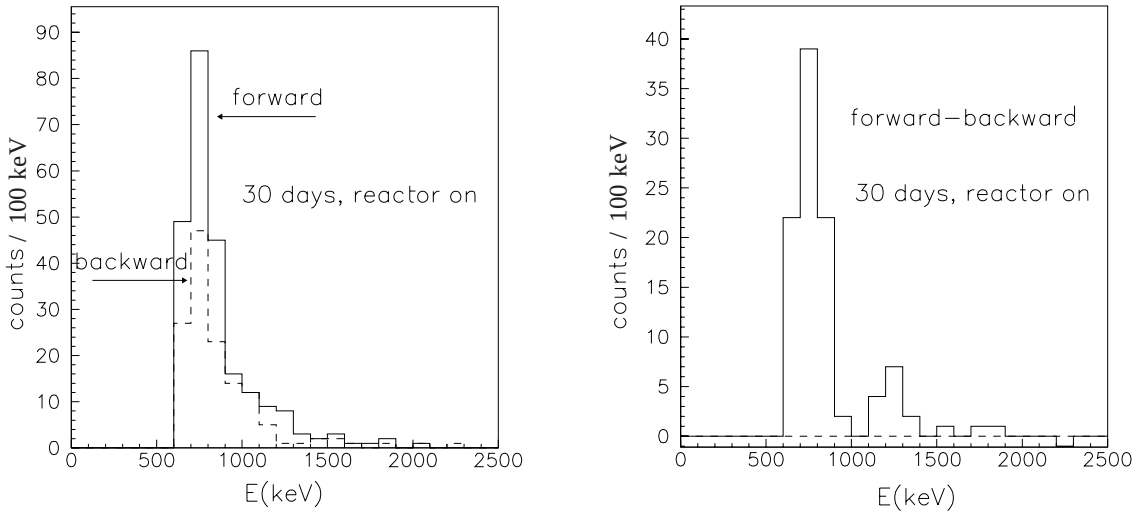

Figure 3.18: *Left: recoil energy distribution of electrons in the TPC for a 30 days run (visual tracking). Right: subtracted plot. The low energy cut is due to the offline threshold cut of 700 keV (the event drop below 700 keV is not sharp because a precise recalibration of the anode pulse height was performed after the cut).*

In the alternative analysis (followed by the University of Zürich group) events are processed using a pattern recognition program ("automatic tracking"). With the automatic reconstruction program we should be able to analyze larger datasets, e.g. neutrino data with lower electron recoil energies. However, the software needs to be carefully tested and compared to Monte Carlo simulation. In fact, some of the early reconstruction algorithms were inappropriate and we had to rewrite part of the reconstruction software. We now describe in more details the analysis of about 24% of the data using the new automatic reconstruction software [3].

The typical TPC trigger rate of 100 Hz was reduced by the anticompton shield (which mostly removed the cosmic muons) to about 0.15 Hz. The size of an event was 600 kB and we collected 1.4 million raw data events on exabyte tapes with reactor ON. The data were first filtered to remove noise on the anode signal and to set a preliminary electron recoil energy threshold of 250 keV. Events with tracks crossing the anode led to fast photomultiplier signals and were removed. The anticompton veto

was applied with a threshold of 100 keV and a first fiducial volume cut was applied to remove events with signals close to the edge of the TPC, i.e. those with signal on the first or last $x-y$-strips (which are perpendicular to the axis z of the TPC).

These cuts led to 2.8×10^5 reactor ON events (and to 8.1×10^4 reactor OFF events) to be further processed by the pattern recognition programme. The point with the largest energy deposit (see fig. 3.17 determines the coordinates of the track endpoint (stopping electron). The track is then reconstructed and the vertex (neutrino-electron scattering point) determined independently in the $x-z$ and $y-z$ projections. The vertex position along z has to agree in either projection within a resolution of 1.4 cm determined by Monte Carlo simulation using GEANT. A new fitting procedure was developed to determine the azimuthal angle ϕ of the electron as the previous approach led to computational instabilities. The electron recoil angle (polar angle Θ) is finally determined knowing the position of the reactor core. The cosΘ (fig. 3.19) distribution is now in much better agreement with the results from the visual tracking. The events are then written to data summary tapes.

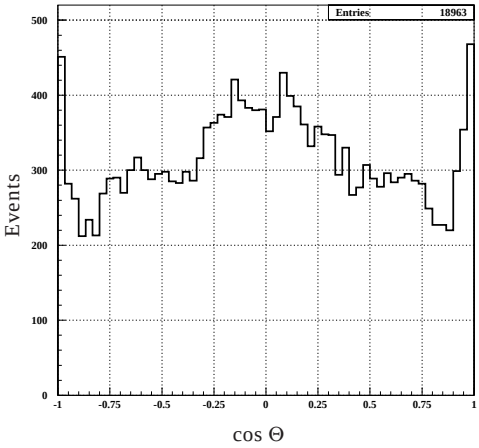

Figure 3.19: *cosΘ distribution of recoil electrons for reactor ON events (not corrected for acceptance). CosΘ = 1 corresponds to the direction opposite to the reactor core.*

This reconstruction procedure was applied so far to 30% of the available 2.8 $\times10^5$ reactor ON events (and to 56 % of the reactor OFF events). Further cuts were then applied: (i) an electron threshold cut of 500 keV, (ii) a fiducial volume cut of 42 cm around the TPC axis and (iii) a drifttime cut ensuring that the track is confined within 40 μsec (the maximum drift time of the TPC), (iv) a positive neutrino energy, reconstructed from the recoil angle and recoil energy. We obtained 160.4 $\pm$ 2.8 events/day in the forward hemisphere (hence opposite to the reactor core) and 155.1 $\pm$ 2.8 events/day in the backward hemisphere. This leads to a forward/backward asymmetry A_{FB} of 5.3 $\pm$ 4.0 events/day (the corresponding asymmetry for reactor OFF events is -4.1 $\pm$ 5.0). Figure 3.20 shows A_{FB} as a function of electron energy. The black curve shows the electroweak prediction with no contribution from the neutrino magnetic moment.

As for the visual tracking at 700 keV threshold, we find about twice as many events as expected . Of course the statistical significance is not yet sufficient to claim a non vanishing magnetic moment, but another 75% of the data remain to be processed. We find from these results a preliminary 90% confidence level upper limit of 2×10^{-10} μ_B. Previous laboratory experiments led to upper limits of $\mu_\nu = 1.9\times10^{-10}$ μ_B [4] and 1.5×10^{-10} μ_B [5]. The astrophysical upper limits, e.g. from SN1987A, are lower by two orders of magnitude but make assumptions, in particular that the neutrino is a Dirac particle. On the other hand, it is interesting to note that a reanalysis of Reines' Savannah data [6] led to a magnetic moment of the size of our upper limit, when taking into account today's improved knowledge of reactor spectra [7].

Data taking for this experiment was completed in autumn 2001. The detector is currently running

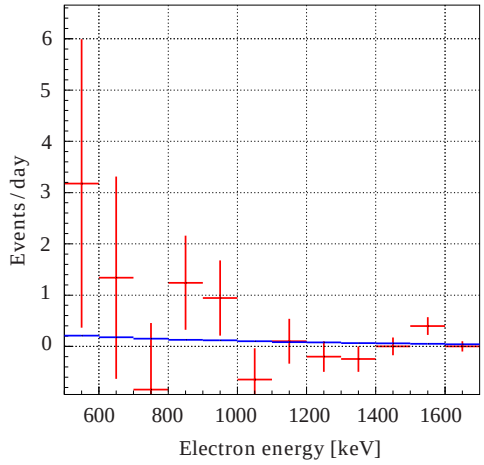

Figure 3.20: *Forward/backward asymmetry A_{FB} as a function of electron energy (red data points). The black curve shows the expected electroweak signal assuming a vanishing magnetic moment.*

at 1 bar, and various calibration are being performed before decommissioning in 2002.

References

[1] C. Amsler *et al.*, Nucl. Instr. Methods **A 396** (1997) 115

[2] M. Avenier *et al.*, Nucl. Instr. Methods in Phys. Research (in print)

[3] O. Link, PhD thesis, Universität Zürich, in preparation

[4] A. I. Derbin *et al.*, JETP Lett. **57** (1993) 768

[5] J.F. Beacom and P. Vogel, Phys. Rev. Lett. **83** (1999) 5222

[6] F. Reines, H.S. Gurr and H.W. Sobel, Phys. Rev. Lett. **37** (1976) 315

[7] P. Vogel and J. Engel, Phys. Rev. **D39** (1989) 3378

3.3 Research group of Prof. C. Amsler

Articles

- Study of f_0 decays into four neutral pions
  A. Abele et al. (Crystal Barrel Collaboration)
  Eur. Phys. Journal C 19 (2001) 667
- 4π-decays of scalar and vector mesons
  A. Abele et al. (Crystal Barrel Collaboration)
  Eur. Phys. Journal C 21 (2001) 261
- Branching ratios for $\bar{p}p$ annihilation at rest into two-body final states
  A. Abele et al. (Crystal Barrel Collaboration)
  Nucl. Phys A 679 (2001) 563
- A High Resolution Search for the Tensor Glueball Candidate $\xi(2230)$
  C. Amsler et al. (Crystal Barrel Collaboration)
  Phys. Lett. B 520 (2001) 175
- Proton-antiproton annihilation at 900 MeV/c into $\pi^0\pi^0\pi^0$, $\pi^0\pi^0\eta$ and $\pi^0\eta\eta$
  C. Amsler et al. (Crystal Barrel Collaboration)
  Eur. Phys. J. C 23 (2002) 29
- Design and test of pixel sensors for the CMS experiment
  G. Bolla et al.
  Nucl. Instr. Meth. in Physics Research A 461 (2001) 182
- Loretz-angle in irradiated silicon
  B. Henrich, R. Kaufmann
  Nucl. Instr. Meth. in Physics Research A 477 (2002) 304
- Antihydrogen Production and Precision Spectroscopy with ATHENA / AD1
  C. Amsler et al. (ATHENA Collaboration)
  "The Hydrogen Atom, Precision Physics of Simple Atomic Systems", ed. S.G. Karshenboim et al., Springer Lecture Notes in Physics, Berlin 2001, p. 469-488
- Proton-antiproton annihilation into $\pi^0\pi^0\pi^0$, $\pi^0\pi^0\eta$ and $\pi^0\eta\eta$ at 900 MeV/c
  C. Amsler
  Proc. of the Int. Workshop XXIX on Gross Properties of Nuclei and Nuclear Excitations, Hirschegg, ed. H. Feldmeier et al., GSI Pub. 2001, p. 18
- The ATHENA Antihydrogen Detector
  C. Amsler
  Proc. Int. Conf. on High Energy Physics, Budapest, Journal of High Energy Physics PRHEP-hep2001 (2001) 174
- New Results in Proton-Antiproton Annihilation and the Status of Glueballs
  C. Amsler
  Proc. Int. Conf. on High Energy Physics, Budapest, Journal of High Energy Physics PRHEP-hep2001 (2001) 270
- Development of Radiation Hard Pixel Sensors for the CMS Experiment
  R. Kaufmann
  Dissertation, Universität Zürich, 2001
- Temperature Dependence of Pure CsI between 77 K and 165 K and the Performance of Wavelength Shifters
  D. Grögler
  Diplomarbeit, Universität Zürich, 2001

- Detection of Antihydrogen with a Si-μ-strip and CsI-Crystal Detector at Cryogenic Temperature
  C. Regenfus
  Proc. of the XXXth Int. Conf. on High Energy Physics, Osaka, ed. C.S. Lim and T. Yamanaka, World Scientific (2001) 1225

Articles in press

- A high resolution silicon beam telescope
  C. Amsler et al.
  Nucl. Instr. Meth. in Physics Research A 480 (2002) 499

- Temperature dependence of pure CsI: scintillation light yield and decay time
  C. Amsler et al.
  Nucl. Instr. Meth. in Physics Research A 480 (2002) 492

- Meson Resonances in Proton-Antiproton Annihilation
  C. Amsler
  Proc. Int. Conf. on the Structure and Interactions of the Photon (PHOTON 2001), Ascona, World Scientific, 2001

- Comment on "Protonium annihilation into $\pi^0\pi^0$ at rest in a liquid hydrogen target"
  C. Amsler et al. (Crystal Barrel Collaboration)
  Phys. Rev. D (2002)

- Sub MeV Particle Detection and Identification in the MUNU Detector
  M. Avenier et al.
  Nucl. Instr. Meth. in Physics Research A (2002)

- Non-$q\bar{q}$ mesons
  C. Amsler
  Eur. Phys. Journal (2002)

- The η(1440), f_1(1420), and f_1(1510)
  M. Aguilar/Benitez, C. Amsler and A. Masoni
  Eur. Phys. Journal (2002)

- Producing Slow Antihydrogen for a Test of CPT Symmetry with ATHENA
  M.C. Fujiwara et al. (ATHENA Collaboration)
  Preprint nucl-ex/0202020
  Journal of Hyperfine Interactions (2002)

- Design, construction and performance of the cryogenic antihydrogen detector for ATHENA
  C. Regenfus
  Proc. 10th Int. Workshop on vertex detectors (VERTEX 2001), Brunnen, Switzerland, 2001

Invited Lectures

- C. Amsler
  Contributed talk, Int. Conf. on High Energy Physics, Budapest, 13.7.01
  "The ATHENA Antihydrogen Detector"

- C. Amsler
  Contributed talk, Int. Conf. on High Energy Physics, Budapest, 13.7.01
  "New Results in Proton-Antiproton Annihilation and the Status of Glueballs"
- C. Amsler
  Invited talk, Int. Conf. on the Structure and Interactions of the Photon (PHOTON 2001), Ascona, 6.9.01
  "Meson resonances in $\bar{p}p$ annihilation"
- N. Madsen
  Contributed talk, 3rd Euroconf. on Atomic Physics at Accelerators (APAC01), Aarhus, 10.9.01
  "Vertical blow up in a low current, stored, laser-cooled ion beam"
- C. Regenfus
  10th Int. Workshop on vertex detectors (VERTEX 2001), Brunnen, 24.9.01
  "Design, construction and performance of the cryogenic antihydrogen detector for ATHENA"
- C. Regenfus
  Seminar, ETHZ, 20.11.01
  "Detection of antihydrogen in the ATHENA experiment with a cold Si-microstrip and a pure CsI detector"

ATHENA Collaboration (2002):
M. Amoretti, C. Amsler, G. Bendiscioli, G. Bonomi, A. Bouchta, P. Bowe, C. Carraro, M. Charlton, M. Collier, M. Doser, V. Filippini, A. Fontana, M.C. Fujiwara, R. Funakoshi, P. Genova, A. Glauser, J. Hangst, R.S. Hayano, H. Higaki, M.H. Holzscheiter, O. Iannarelli, L. Jorgensen, D. Kleppner, V. Lagomarsino, R. Landua, C. Lenz Cesar, D. Lindelf, E. Lodi-Rizzini, M. Macri, N. Madsen, G. Manuzio, M. Marchesotti, P. Montagna, H. Pruys, C. Regenfus, P. Riedler, A. Rotondi, G. Rouleau, P. Salvini, G. Testera, D.P. van der Werf, A. Variola, T. Watson, T. Yamazaki, Y. Yamazaki

CRYSTAL BARREL Collaboration (2001):
C. Amsler, C.A. Baker, B.M. Barnett, C.J. Batty, M. Benayoun, A. Berdoz, P. Blüm, K. Braune, T. Case, K.M. Crowe, M. Doser, W. Dünnweber, D. Engelhardt, M.A. Faessler, P. Giarritta, R.P. Haddock, F.H. Heinsius, M. Heinzelmann, N.P. Hessey, P. Hidas, D. Jamnik, H. Kalinowsk, B. Kämmle, P. Kammel, J. Kisiel, E. Klempt, H. Koch, M. Kunze, U. Kurilla, M. Lakata, R. Landua, H. Matthäy, C.A. Meyer, F. Meyer-Wildhagen, L. Montanet, R. Ouared, K. Peters, B. Pick, M. Ratajczak, C. Regenfus, W. Roethel, U. Strohbusch, M. Suffert, J.S. Suh, U. Thoma, I. Uman, S. Wallis-Plachner, D. Walther, U. Wiedner, K. Wittmack, Č. Zupančič.